EUROFUSION WPJET1-PR(15) 13079

T Makkonen et al.

Combined ERO, DIVIMP, and EDGE2D-EIRENE simulations of material migration in ELMy H-mode JET plasmas

Preprint of Paper to be submitted for publication in
Plasma Physics and Controlled Fusion

This work has been carried out within the framework of the EUROfusion Consortium and has received funding from the Euratom research and training programme 2014-2018 under grant agreement No 633053. The views and opinions expressed herein do not necessarily reflect those of the European Commission.

Combined ERO, DIVIMP, and EDGE2D-EIRENE simulations of material migration in ELMy H-mode JET plasma

T. Makkonen[1], M.I. Airila[2], S. Brezinsek[3], M. Groth[1], A. Järvinen[1], and JET contributors*

EUROfusion Consortium, JET, Culham Science Centre, Abingdon, OX14 3DB, UK
[1] Department of Applied Physics, Aalto University, PO Box 14100, FI-00076 AALTO, Finland
[2] VTT Technical Research Centre of Finland, PO Box 1000, FI-02044 VTT, Finland
[3] Forschungszentrum Juelich Gmb, Institut fr Energie- und Klimaforschung — Plasmaphysik, 52425 Jlich, Germany
* See the Appendix of F. Romanelli et al., Proceedings of the 25th IAEA Fusion Energy Conference 2014, Saint Petersburg, Russia

Abstract

ERO, DIVIMP, and EDGE2D-EIRENE simulations were used to interpret material migration studies with ^{13}C tracer in JET with the carbon wall. The experiment was done by injecting isotopically labeled methane, $^{13}CH_4$, into the common flux region at the outer target. The injected carbon was experimentally found to have migrated to the inner target and the private flux region. The role of various migration mechanisms, including the role of ELMs, on the final deposition pattern was studied numerically. Two key mechanisms explaining the observed pattern were identified: transport from the far outer target to the inner via the main SOL and core, erosion at the inner target, aided by ELMs, transporting injected carbon to the private flux region.

1 Introduction

Migration of impurities in tokamaks has to be understood to maximize plasma facing component (PFC) lifetime and to minimize tritium retention as well as core contamination — these issues are critical for ITER. Several key parameters impacting large-scale impurity migration have been identified and are listed in e.g. [1] or [2] and references therein. These include physical and chemical erosion [3][4][5], surface morphology effects such as roughness [6], scrape–off–layer (SOL) conditions and specifically the parallel flow [7], and 3D effects [8]. However, when combined, these effects produce a very complex system that is is difficult to accurately predict. One way to reduce the complexity is to control the location of the impurity source, control the plasma conditions, and

constrain the experimental time to limit the amount of re–erosion. To address these issues, several tracer injection experiments have been performed in various tokamaks, see e.g. [9] for TEXTOR, [10] for JET, [11] and [12] for ASDEX Upgrade, [13] for DIII–D, or [14] for JT-60U. A comprahensive review is found in [1]. In these tracer experiments, an isotopically labeled tracer, typically ^{13}C or ^{15}N, is injected at a well specified location and the resulting surface deposition is measured post–mortem. This method links the source and destination of the impurity more unambiguously to each other than campaign–integrated measurements. Controlled tracer injection experiments allow interpretation of the migration by modelling, and subsequently, achieving predictive power as the experimental databases, numerical tools, and theoretical understanding build up.

This paper focuses on experimental data gathered during 30 similar discharges (JET pulse numbers 79816—79853) at the end of the 2009 JET campaign, when the JET first wall was made of carbon fibre composite (JET–C). The experimental results are reported in [15]. In total, 3.30×10^{23} atoms of ^{13}C were injected from the outer diverter in the near scrape–off layer at $R = 2.82$. This location maps to $R - R_{\mathrm{sep,\ OMP}} = 2$ cm at the outer midplane. The injection was from 24 valves located toroidally periodically at the poloidal location shown in figure 1. The injection occurred during 132 s of plasma time resulting in an average puffing rate of 1.0417×10^{20} per second per valve. In reality a fraction, up to 1/3, could have been lost to the AGHS. However, the number stated above is used in these simulations to be consistent with previous work [15]. The discharges [15] in H–mode confinement with ELMs (edge localized modes) were 2.5 T, 2.5 MA in deuterium with $< n_e >_{\mathrm{core}} = 5.9 \times 10^{19}$ m^{-3}, $< n_e >_{\mathrm{edge}} = 3.6 \times 10^{19}$ m^{-3}, and $n_{\mathrm{gw}} = 65$ %. The $\vec{B} \times \nabla B$ direction was into the lower divertor. The amount of injected methane is likely to perturb the local plasma conditions. This has not been accounted for in the simulations, however.

Post–mortem analysis of the surface tiles [15] revealed strong local deposition close to the injection location as well as much of the injected carbon traveled from the outer divertor to the inner target and the PFR. The transport of injected carbon to the inner target is consistent with what has been observed in campaign integrated studies [16].

The migration pathways were preliminary studied in [15] using the same set of codes as in this paper, ERO [17], DIVIMP [18] , and EDGE2D-EIRENE [19, 20]. The DIVIMP results suggested transport from LFS to the HFS along the SOL and core as the key mechanism bringing carbon from the outer target to the inner target. However, the role of erosion in the large-scale impurity migration was not studied and the publication did not address how the carbon deposits at the PFR. Also, the codes were used separately from each other in [15].

In the present work we take benefit of the strengths of each of the three codes by running them in an integrated manner. EDGE2D-EIRENE is used to produce the plasma background required by the trace impurity codes, ERO

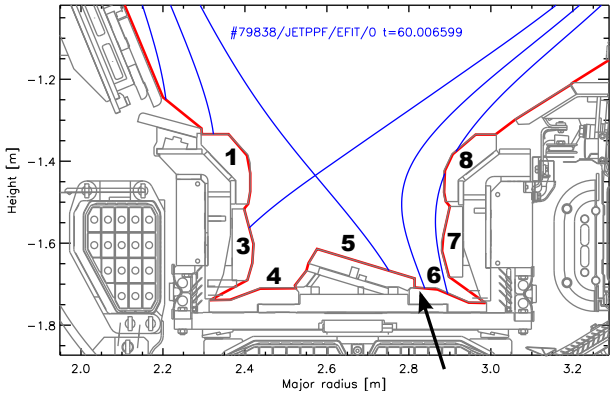

Figure 1: The geometry of the JET divertor during the experiment and magnetic geometry from the discharge #79839. The tile numbers are shown. The injection location is marked by the black arrow pointing on tile 6.

is used to study transport and erosion of ^{13}C in the divertor, and DIVIMP is used for the main chamber transport of ^{13}C. Typically, DIVIMP models impurity transport in the entire tokamak but in this work it was used only in the main chamber. The extensive plasma-surface interaction, atomic and molecular physics models and databases of ERO provide sufficient physical accuracy locally, while DIVIMP extends the model to the global scale that is currently not possible using ERO alone. Using this set of codes, and the plasma physics they employ, we aim to reproduce the observed deposition pattern and shed light on the most important pathways of ^{13}C migration in this experiment. More specifically, this paper addresses the following questions:

- What is the relative importance of transport across the divertor legs versus transport through the main SOL and core?
- What is the role of re-erosion and short–range, step–wise migration (walking) [28][29]?
- What is the effect of ELMs in terms of erosion and carbon transport?

These questions will be studied in a stepwise manner. Firstly, only transport across the divertor is accounted for. Secondly, the role of main chamber transport is investigated. Thirdly, a model to address the impact of ELMs on erosion, transport, and deposition is introduced. Finally, some of the uncertainties in the model connecting ERO and DIVIMP are probed. Also, the rate of erosion of wall carbon and re-erosion of injected tracer carbon are investigated. In doing so, various assumptions for the erosion model are tested.

Preliminary results of this work have been included in the review article [2]. The purpose of the present contribution is to describe in sufficient detail the novel external transport option developed for ERO and discuss the refined

calculations carried out since the publication of [2]. The qualitative picture is consistent with [2].

2 Simulation setup

The carbon migration simulations were accomplished with a combination of the EDGE2D-EIRENE, ERO, and DIVIMP codes. The geometry of the experiment and the computational domain of each code is shown in figure 2. EDGE2D-EIRENE is used to create the plasma backgrounds for ERO and DIVIMP. This plasma background contains the densities and temperatures of electrons, ions, and various impurity species, as well as the flow velocity of the plasma and the electric field. ERO is used to simulate impurity transport and erosion in the divertor while DIVIMP is used to simulate carbon transport in the main SOL and core. Both codes treat the injected ^{13}C as a trace element. ERO and DIVIMP were integrated by implementing a new *external transport option* into ERO where particles exiting the simulation volume across the top boundary are either lost or re-introduced with the new position obtained with the help of a transport matrix as explained in section 2.3. In this work, the transport matrix is calculated using DIVIMP but other methods could be used as well (e.g. ASCOT [8]). The approach in this paper has similarities to what is used in e.g. the Walldyn code package [30]. In Walldyn, DIVIMP is used to calculate a transport matrix indicating how much of eroded material is transported between various wall tiles. Here, the transport matrix is used to indicate how much of the injected ^{13}C that escapes into the main chamber re-enters back to the lower divertor and in what radial location.

The used setup is not applied to study 3D effects (see e.g. [8]) since DIVIMP and EDGE2D-EIRENE are toroidally symmetric and the 3D code ERO is provided with a toroidally symmetric wall geometry and plasma background. We assume that 3D effects are not likely to play a significant role in these experiments since the injection is toroidally periodic (24 valves) and all the measurement points are located on the toroidally symmetric lower divertor region. In reality, the deposition is toroidally periodic [15].

2.1 Plasma modelling with EDGE2D-EIRENE

To calculate the 2D distributions of the plasma parameters, including n, T_e, T_i, $u_\parallel$, E, the 2-D multi-fluid code EDGE2D/EIRENE [19][20][21] was set up for a steady-state, inter-ELM time-slice. The input power to the computational domain was setup equal to the estimated power crossing the separatrix between ELMs: 10 MW. This is calculated by subtracting the radiative power losses within the confined plasma, 1.5 +/- 0.5 MW, and the rate of the change of the plasma stored energy between ELMs, 3.5 +/- 0.5 MW, from the total neutral beam heating power in the experiment, 15 MW.

Anomalous radial transport coefficients for particle diffusion and electron and ion heat conduction were adjusted to reproduce the experimentally mea-

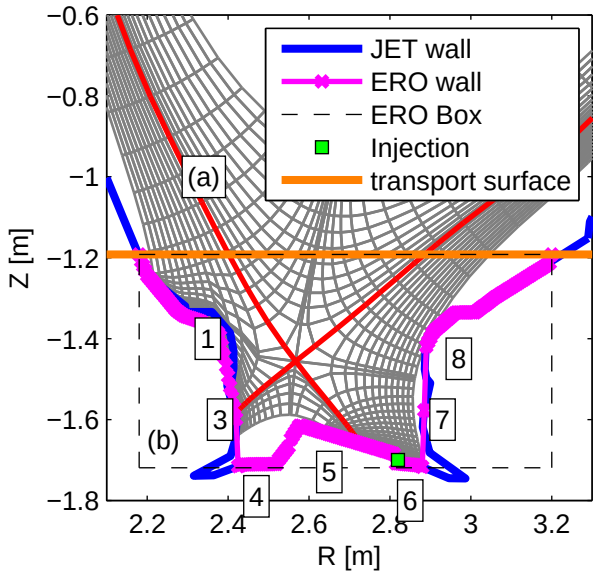

Figure 2: The computational domain of (a) EDGE2D-EIRENE and DIVIMP, and (b) ERO. Particles crossing the top boundary in ERO are reintroduced into the ERO simulation volume or lost according to DIVIMP predictions of main SOL and core transport. The surface combining ERO and DIVIMP is marked in the figure as the transport surface. Due to computational limitations, the exact JET wall shape has been simplified, as is shown in the figure. Implications are discussed in the text. The divertor tiles are marked in the figure.

sured profiles of electron density and temperature at the outer mid-plane. The background plasma carbon content was calculated self-consistently by assuming physical sputtering of the carbon plasma-facing components according to Eckstein yields [22] and chemical sputtering according to the Roth/Pacher (2003) [23] for the wall. The Roth/Pacher model has a flux dependant sputtering yield (sputtered particles per incoming ion) and this was assumed to be a fixed 10^{19} $m^{-2}s{-}1$. The carbon chemical sputtering was enhanced by a factor of 2 to reproduce the measured radiated power. However, as a result, the outer divertor CIII (465 nm) emission is overestimated by a factor of 2 in the simulations, indicating that the extra carbon produced by enhanced sputtering in the simulations compensates a short fall of radiation due to other processes in the plasmas [24]. The simulated carbon radiated power was of about 1.4 MW and simulated deuterium radiation of about 0.2 MW, while the measured divertor radiation in the experiment was of about 1.4 +/- 0.5 MW. The resulting simulated outer target power deposition was around 6 MW consistent with experimental values measured with the infrared camera, 5 +/- 1 MW. The specroscopic data gathered by the Ks3 system is shown in figure 3.

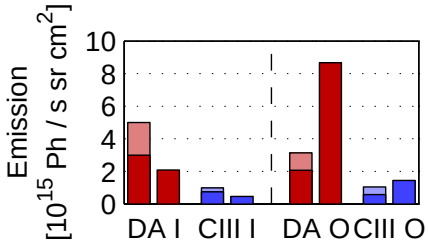

Figure 3: Emission intensity of D_α ("DA") and C III ("CIII") from the KS3 spectroscopic system for the inner ("I") and outer targets ("O"). The error bars of the measurements are shown. The value predicted by EDGE2D (no error bars) is on the right of each measurement.

The simulated upstream density was adjusted to reproduce the experimentally measured outer divertor conditions in terms of electron temperature and density, shown in figure 4. The best match was obtained with an upstream electron density of 2.67×10^{19} m^{-3}. The simulated peak electron temperature at the low field side divetor target, 60 eV, was within a factor of 1.4 from the experimental values measured by divertor target Langmuir Probes, 45 eV, and the simulated peak outer target electron density, 6×10^{19} m^{-3}, was within a factor of 2 from the experimental values, 3×10^{19} m^{-3}. At the inner target the strike point was located close to the boundary of the JET divertor tiles 1 and 3. Therefore, the diagnostic coverage of the inner divertor profiles is compromised by the gap between tiles for which the profiles cannot be obtained (fig. 4). However, these simulations were conducted without cross-field drift terms due to numerical stability reasons; hence, the densities in the inner divertor volume are presumably underestimated and the electron temperatures correspondingly

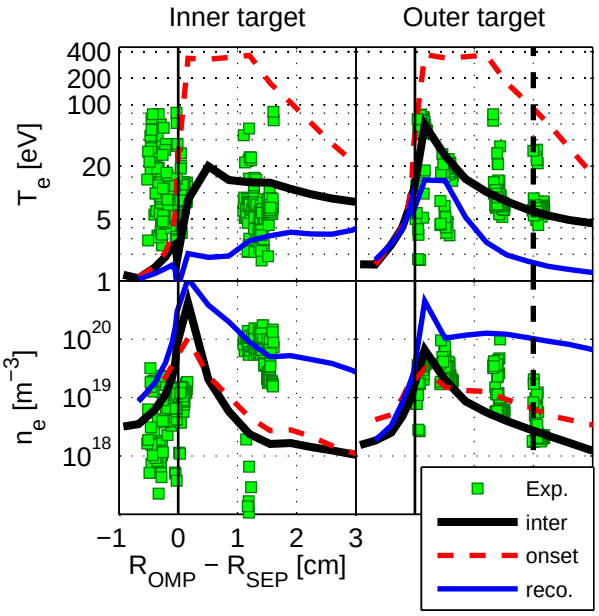

Figure 4: Outer (right) and inner (left) target density (bottom) and temperature (top) profiles. The vertical dashed line indicates the injection location. "Inter" refers to the inter ELM plasma solution while "onset" and "reco." refer to the ELM onset and the ELM recovery phases, respectively.

overestimated. The impact of cross-field drift terms on the SOL plasmas solution have been investigated in [27], [24], and references therein.

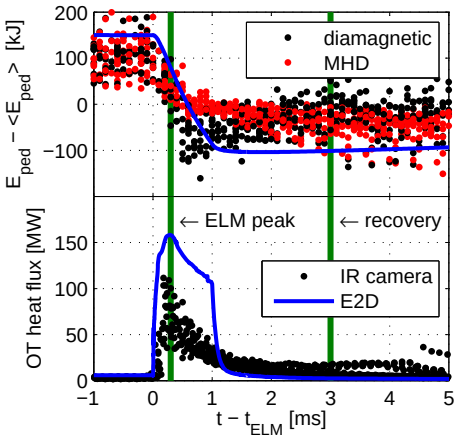

Figure 5: The drop in stored energy (top) during an ELM and the resulting OT heat flux (bottom) as a function of time. The two vertical green lines indicate the time slices used for the ELM onset plasma background and the ELM recovery plasma background. The solution before $t \leq 0$ s is the inter ELM plasma background.

To investigate the impact of 20—30 Hz ELMs on the divertor conditions and transient erosion, transport, and deposition dynamics, a single ad-hoc ELM was simulated based on the obtained steady state, inter–ELM simulation following the recipe in [25][26]. To impose an ELM in the simulations, ad hoc enhancement of the cross-field diffusion and heat conduction around the outer mid-plane pedestal for a 1 ms time-slice was conducted.

To mimic ELMs, the cross-field diffusion was multiplied by a factor of 200, and the cross-field ion heat conductivity by a factor of 200 and the electron heat conductivity by a factor of 75. The ELM enhancement domain was limited radially between R_{omp} - R_{sep} between -9 cm and 1 cm and poloidally between Z = -0.8 and Z = 1.1m. The ELM simulations were time dependent in EDGE2D. The resulting ELM size was about 250 kJ representing the upper range of the experimentally measured values (fig. 5). The resulting power flux at the outer target was overestimated by a factor of 1.5 during the early part ELM (0 — 0.3 ms after the ELM onset) and a factor of 2 during later part of the ELM (0.3 — 1 ms after the ELM onset).

Besides the inter–ELM plasma solution, the trace particle simulations employed the plasma solution from the ELM peak period as well as a plasma solution after the ELM (ELM recovery). These time slices are shown in figure 5. The plasma conditions during the inter–ELM, ELM peak, and ELM recovery phases differed not only at the target (fig. 4) but also in the main SOL (fig. 6). The poloidal profiles for density, temperature, and flow velocity are shown

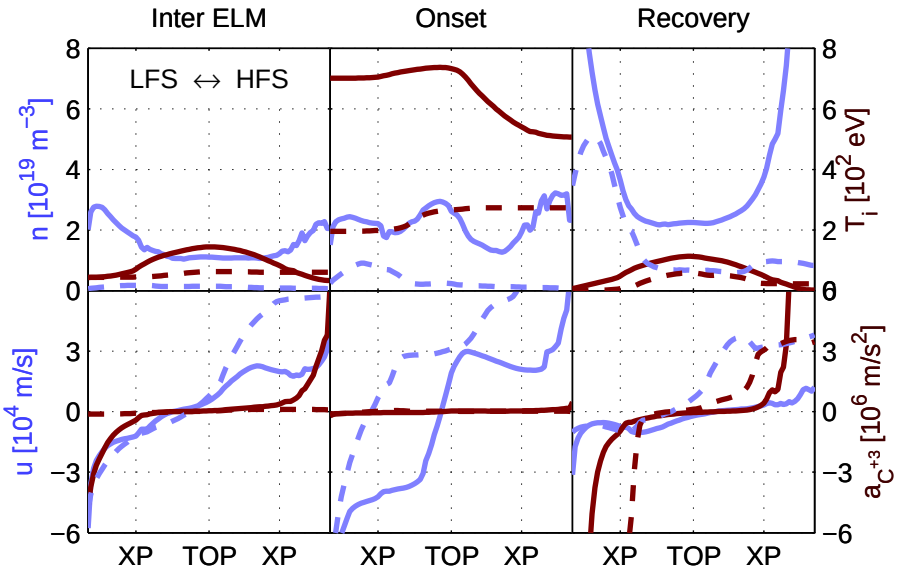

Figure 6: Poloidal density, temperature, and flow profiles for the inter ELM plasma solution (left column), the ELM onset plasma solution (middle column), and the ELM recovery plasma solution (right column). The top row displays densities (light blue lines) and temperatures (dark red lines) for the near SOL (solid lines, $R - R_{sep} = 0.5$ cm) and the far SOL (dashed lines, $R - R_{sep} = 4$ cm). The bottom row shows the flow velocities for the near SOL (solid light blue) and the far SOL (dashed light blue). The acceleration of C^{+3} in the parallel–B direction is also shown in dark red. The acceleration is calculated for a stationary ion using the flow velocity and the Spitzer stopping time. The x–axis of each plot is approximately the normalized poloidal distance along the field lines. The locations of the LFS X–point, the top of the machine, and the HFS X-point are marked. Positive values for the flow velocity and acceleration are towards the inner target.

in figure 6 for the three plasma solutions. These poloidal profiles are shown for two radial locations: close to the separatrix ($R_{\mathrm{OMP}} - R_{\mathrm{SEP,OMP}} = 0.5$ cm) and in the far SOL ($R_{\mathrm{OMP}} - R_{\mathrm{SEP,OMP}} = 4$ cm). Furthermore, since collisionality determines the coupling between the deuterium flow and the impurities, the acceleration of C^{+3} ions at rest is also plotted using

$$a = u_{\mathrm{bg}}/\tau_{\mathrm{s}} \tag{1}$$

where u_{bg} is the background flow velocity and τ_{s} is the Spitzer stopping time for the given density, temperature, plasma ion mass, impurity ion mass, and impurity ion charge. Negative values for the flow velocity and the acceleration are towards the outer target and positive values are toward the inner target.

In comparison to the inter ELM plasma solution, the ELM onset plasma solution is very hot and less dense. In the ELM recovery phase, the plasma is cooled but the density is considerably larger. For impurity transport this means that carbon is collisionally less coupled to the background flow during the ELM onset period. This can be seen in figure 6 where the acceleration to carbon ions is negligible during the onset period even though the background flow is larger compared to the inter ELM period. The situation is reversed for the ELM recovery period. Carbon impurities are well coupled to the dense, cool plasma and are predicted to flow towards the targets.

The inter ELM EDGE2D plasma solution matched outer midplane measurements as well as Langmuir probe measurements at the inner and outer target (fig. 4). The electron temperature at both targets is well above the sputtering treshold meaning small discrepancies do not strongly affect the erosion/deposition balance. The predicted SOL plasma flow profile is not consistent with experimental measurements [7], however. The SOL flow is predicted to be close to zero at the top of the SOL while measurements show a strong flow towards the inner target.

2.2 Impurity migration modelling with ERO and DIVIMP

Impurity tracing was accomplished with a combination of the ERO [17] and DIVIMP [18] codes. ERO is versatile tool that follows the full orbits of trace particles (molecules, atoms and ions) in a given background and geometry. Following charged particles, ERO utilizes a static 3D magnetic field and a 3D electric field. In the present study, both fields were assumed toroidally symmetric. ERO takes into account Coulomb collisions with the background plasma, including higher order corrections for the temperature gradient force. For impurity tracing, ERO utilizes the predicted (or measured) density profile, ion and electron temperature profiles, the parallel plasma flow, parallel temperature gradients, and radial and poloidal electric fields given in 2D by a suitable external model (here, EDGE2D-EIRENE).

Molecular and atomic reactions are included in ERO. The break–up of CH_4 is modeled using data from [31], and the ionization and recombination of C using ADAS data [32].

ERO features a rich set of plasma–surface interaction physics and chemistry. Erosion of the wall is caused by physical and chemical erosion by the plasma background as well as the injected impurities themselves. In these simulation, physical erosion is modeled by the Bohdansky–Yamamura formula, and chemical erosion is given by the Roth formula (see ref. [33] and references therein). The temperature of the surface affects the chemical erosion yield. It was assumed to be a constant 300 °C in the simulations. In reality the surface temperature varied spatially and temporally during the discharges. The temperature at the outer strike point reached values up to 1500 °C during ELMs and at the end of the discharges. Elsewhere, the assumption of 300 °C is consistent with experimental measurements. The variation in the surface temperature is not taken into account in these simulations and is thus a source of error. However, the total erosion yield as a function of surface remperature stays well within a factor of two between 200 and 1250 °C [5]. Furtermore, the parameters affecting the erosion rates are scanned in the simulations compensating for this uncertainty.

The concentration of material on plasma-facing surfaces in ERO is modeled using the interaction layer approach [17]. In this model, it is assumed that the impurities on a surface are approximately evenly distributed withing this interaction layer. In this work, values between 20 nm and 60 nm are assumed corresponding to typical ion ranges in the material. The order of magnitude is consistent with previous experimental measurements [28] concerning CH_4 injection in all-carbon JET. In reality, the depth profile of ^{13}C is not uniform toroidally and poloidally and varies in the range of 10 nm—100 nm [28]. The depth of this interaction layer essentially determines how quickly the injected carbon is eroded from the walls due to the incoming hydrogenic flux. Furthermore, enhanced re-erosion of has been observed for carbon [34][35]. In this work we used values between 5 and 40 to address this issue.

Methane was launched in ERO at approximately $R = 2.81$ m and $Z = -1.7$ m with a Maxwellian energy distribution of 0.05 eV corresponding to approximately 300 °C. This is the same as the assumed wall temperature. The angular distribution was cosine. The paths of the neutrals and charged impurity particles were followed in the plasma until wall impact or hitting the computational boundary at $Z = -1.19$ m. We assumed that CH_x molecules hitting the walls were reflected as neutral CH_4 with a 90 % probability, as done in previous work [36]. Carbon atoms and ions striking the walls were assumed to stick to the walls with a 100 % probability. This is justified by the fact that carbon is non–recycling.

The ERO simulations were done for a 15 degree toroidal sector (24 toroidally periodic injection locations) and toroidally periodic boundary conditions were applied. Particles exiting the simulation volume at $Z = -1.19$ m were treated by the external transport option implemented into ERO for this work. This allows to take approximately into account particles escaping into the main SOL and core. The details of this model are described in section 2.3.

Anomalous radial transport is modeled by spatial diffusion in ERO. A diffusion coefficient of 1 m^2/s is used in all the simulations in this paper. This value is consistent with values used for the hydrogenic background plasma in

EDGE2D for these cases as well as experimental measurements of radial impurity transport [37].

2.3 Using DIVIMP as an external transport model for ERO

DIVIMP was used to calculate carbon transport in the main SOL and core using the density, temperature, parallel plasma flow, parallel temperature gradients, and parallel electric fields from EDGE2D-EIRENE. DIVIMP does not include cross field drifts and the radial electric field from EDGE2D is therefore not used. The perpendicular transport is assumed to be dominated by anomalous transport and modeled by pure diffusion. The spatially constant diffusion coefficient of 1 m^2/s was used in all simulations, as in ERO.

The DIVIMP results were used to generate a transport matrix for each EDGE2D-EIRENE plasma solution (inter-ELM, ELM-onset, and ELM-recovery phase). Particles were initialized in DIVIMP at $Z = -1.19$ m with a random R location inside the grid with thermal speed away from the targets and followed until they exited the grid or crossed the surface $Z = -1.19$ m again. The initial (R_{init}) and final (R_{final}) values were stored, as well as a flag indicating whether the particle crossed $Z = -1.19$ m or exited the grid in the main chamber.

The Z-surface was divided into 30 elements and a 30×30 transport matrix (or re-distribution matrix) was calculated using

$$a_{ij} = \text{count}(\text{crossed and } R_{\text{final}} \in I_i \text{ and } R_{\text{init}} \in I_j)/\text{count}(R_{\text{init}} \in I_j) \qquad (2)$$

where count(criterion) refers to the number of test particles satisfying the given criterion. A test particle in ERO exiting the top boundary is either lost or reintroduced according to the data in the transport matrix. If a particle exits the boundary in the interval I_j, it is re-introduced with the probability a_{ij} in the interval I_i. A particle exiting the boundary in the interval I_j is not re-introduced with probability

$$p_{\text{lost, j}} = 1 - \sum_i a_{ij} \qquad (3)$$

meaning it is depodited in the main chamber. Particles deposited in the main chamber in these simulations are no longer followed and cannot be re–eroded. When particles are reintroduced in ERO, it is assumed they are thermalized with the background flow and temperature. For a more rigorous treatment regarding the velocity distribution of re-entering particles, refer to [38].

The transport matrix given to ERO determines how particles exiting the top boundary are treated, and thus affects the final deposition of injected ^{13}C. Figure 7 shows one row of the transport matrix for all three plasma backgrounds. This specific row, number 24, corresponds to impurity particles exiting the simulation volume in the outer SOL. The data in figure 7 shows the probability distribution of re-entry. This location corresponds to where a large fraction of the injected carbon exits the simulation volume, as can be later seen in figure 13.

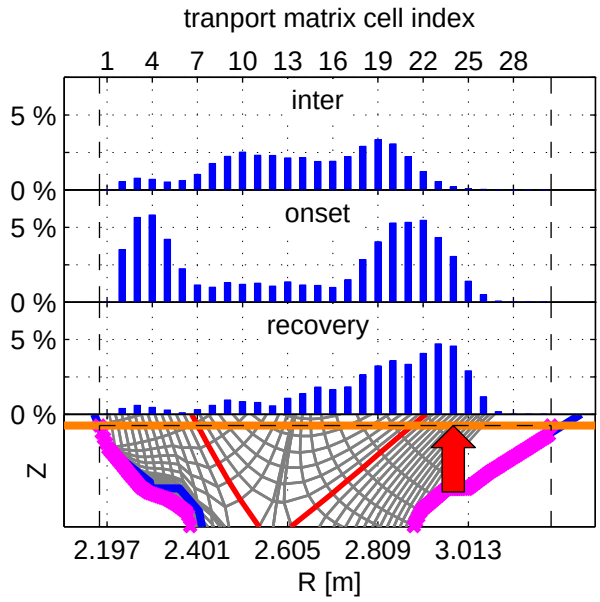

Figure 7: One row of the transport matrix for the inter ELM plasma background (top), the ELM onset background (middle), and the recovery phase background (bottom). This data shows the re-entry probability distribution for particles exiting at the location indicated by the red arrow (cell index 24). The discrete values indicate the probability of reaching the specific cell.

Significant differences are predicted in the transport matrices for the three plasma backgrounds (only one row is shown here). In the hot and sparse ELM onset plasma backgrounds, carbon impurity particles are weakly coupled to the plasma background flow and more easily reach the inner target. Also, the probability of getting deposited in the main chamber is smaller due to spending a shorter period there. For the cool and dense recovery phase, the impurities are predicted to be strongly coupled to background flow. Impurities exiting the top boundary in the outer SOL are most likely to re-enter there being driven back to parallel flow shown in figure 6. It should be, however, pointed out that the predicted parallel flow profiles are not fully consistent with measurements [7].

The limited computational grid in DIVIMP affects the transport matrix. Particles exiting from grid cell 27 and higher are automatically lost. Also, no particles re-enter from these grid cells. The thin computational grid is also likely to overestimate the fraction of particles deposition in the main chamber.

3 Results

3.1 Transport inside divertor

To study the importance of transport inside the divertor, the external transport option was turned off and particles entering the core or main SOL were lost in ERO. The inter-ELM plasma background was used. ^{13}C particles were launched from the injection valve at the outer target in ERO and they were transported in the plasma and either deposited on the walls or lost at the top boundary. Physical and chemical erosion were enabled allowing the primary deposition profile to evolve in time for 150 s, corresponding approximately to the experimental time. The deposition curves are typically not in steady state after 150 s. Three cases were run in ERO using different values for the parameters affecting erosion. The low re–erosion case used an interaction layer of 60 nm and an enhanced re–erosion factor of 5. The medium re–erosion case used values of 20 nm and 5 while the high re–erosion case used values of 20 nm and 40.

Most of the injected carbon was deposited close to the injection location or on the outer baffle (fig. 8) after 150 s of injection and re–erosion. For the low re–erosion case, 94 % was deposited on the outer target and baffle. For the high re–erosion case, this number was 84 %. The normalized deposition at the inner target and private flux remained two or three orders too low using this setup and the total deposition at the inner target and private flux region combined remained below 1 % in total in all cases. The final deposition pattern was qualitatively similar between all three ERO cases. Quantitatively, using high re–erosion decreased outer baffle deposition and increased inner target and private flux region deposition.

The normalized deposition profile at the outer target decreased by approximately 10 % during the 150 s of simulated methane injection. However, the

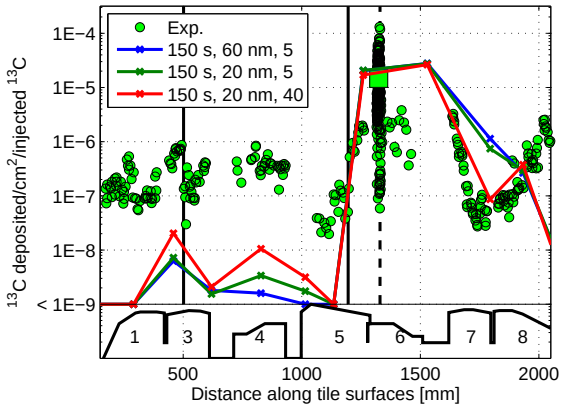

Figure 8: Normalized deposition profiles after 150 s of injection, deposition, re-erosion, and re-deposition. The blue curve uses an interaction layer depth of 60 nm, the green curve uses 20 nm, and the red curve uses 20 nm. The enhanced re-erosion factors are 5, 5, and 40, respectively.

normalized deposition profile at the outer baffle, the inner target, and the private flux region evolved noticeably in time and the the normalized deposition profile after 150 s is considerably different from the primary deposition of injected carbon. For the inner target and private flux region, the difference is at least one order of magnitude. The difference for the outer baffle is approximately one order of magnitude. The simulation case in figure 9 is the one with the highest amount of re-erosion (interaction layer depth of 20 nm, enhanced re-erosion of 40). The qualitative picture was the same in all three ERO cases but most visible for high re–erosion.

The final deposition pattern as well as the evolution in time can be understood by observing the fluxes of injected carbon and eroded wall carbon. The flux of injected carbon is shown in figure 10 (A). The flux of eroded wall carbon shown in figure 10 (B), and is separated to physically eroded carbon in figure 10 (C) and chemically eroded carbon in figure 10 (D). The data in these figures, and subsequent figures 13 and 14, are generated using methods documented in [39]. The fluxes of physically and chemically eroded wall carbon are different due to a different erosion profile, the difference in the energy distribution of the sputtered particles, and different plasma conditions.

Physical erosion dominates at the outer divertor close to the strike point where the plasma is hot. Physically sputtered particles at the outer divertor are likely to be transported further outward, towards tiles 7 and 8, and towards the main SOL. Physically sputtered particles from the outer private flux region are likely to be transported to the inner divertor. Chemical erosion dominates close to the inner strike point where the plasma is very dense and below 10 eV and the hydrogenic fluxes are high. There are also strong sources at the outer baffle

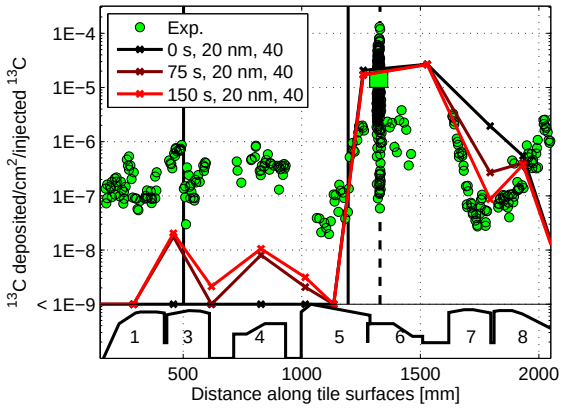

Figure 9: Normalized deposition profiles assuming no main SOL and core transport for the primary deposition (black), and after 75 s (dark red) and 150 s (red) of erosion + continued injection. The inter-ELM plasma background was used. This is the simulation case assuming the highest amount of re-erosion.

and chemical erosion at the outer strike point. Chemically eroded particles at the inner divertor are likely to be transported towards the private flux region. Chemically eroded particles around tiles 7 and 8 are likely to be transported towards the main SOL.

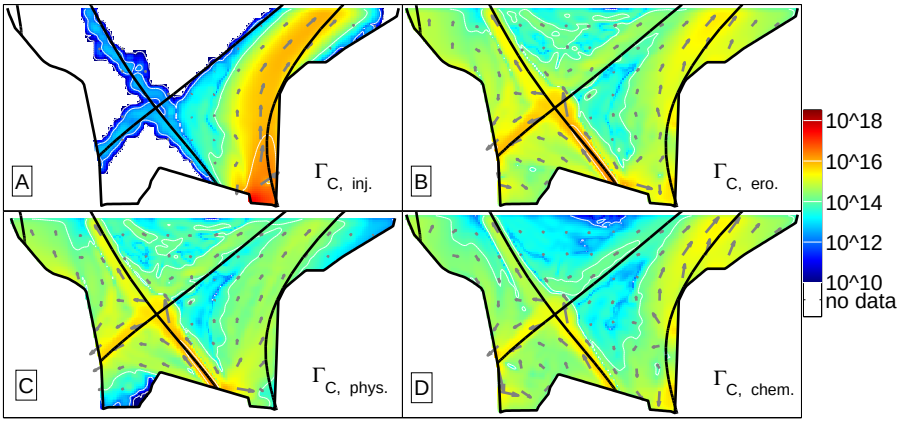

Figure 10: Poloidal fluxes of (a) injected carbon, (b) eroded wall carbon, (c) physically eroded wall carbon, and (d) chemically eroded wall carbon for the inter ELM plasma with no main SOL and core transport. The flux in picture (b) is (c) + (d). The fluxes are in units of 1/cm^{2}s. All flux pictures use the same color scale in this paper.

The primary deposition occurs predominantly on the outer target and the outer baffle (figs. 9 and 10 A). A flux of the injected carbon is directed towards the main SOL (fig. 10 A) and lost at the boundary indicating the need to include main chamber transport. A few test particles are seen in fig. 10 (A) to radially diffuse towards the separatrix and deposit at the inner target close to the strike point. These quantities are, however, very low, in the order of magnitude of 1 particle in 10,000. The increase in normalized inner target deposition in time is due to re–erosion of injected carbon.

The dip in the deposition profile between tile 7 and 8 is explained by chemical erosion. A large fraction of the injected carbon is directly deposited in this region, as seen in figure 10 (A). However, this region also displays strong chemical erosion sources, as seen in figure 10 (D), while physical erosion is of less importance. Increasing erosion yields, either by making the simulation reach steady state faster by decreasing the interaction layer or by increasing the enhanced re-erosion, does not affect the amount of primary injected carbon deposited here but, obviously, increases erosion. The net effect is that smaller deposition in the region between tile 7 and 8.

The deposition predicted by ERO is toroidally symmetric except close to the injection valve, on tile 6. The toroidal deposition profile on tile 6 is toroidaly peaked at the injection location both experimentally and in ERO simulations. However, ERO overestimates the deposition on tile 6 by about a factor of two. The toroidal experimental deposition pattern is shown in figure 11 together with the low re–erosion ERO simulation case. The predicted ERO deposition on tile 6 does not change significantly between ERO simulation cases.

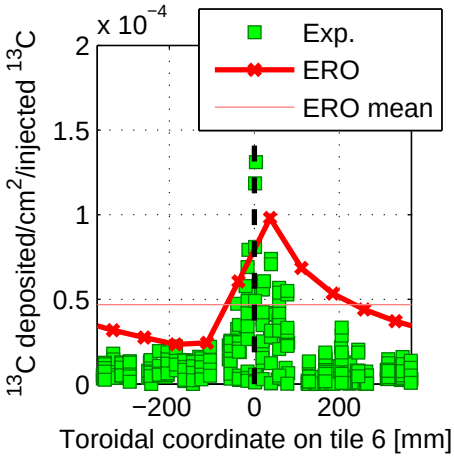

Figure 11: Toroidal deposition profile on tile 6. The positive direction is in the direction of the magnetic field lines. The ERO deposition has been poloidally averaged around tile 6. The scatter in the experimental data represents real scatter as well variations poloidally on tile 6.

3.2 Main chamber transport

To understand the role of main chamber transport, the external transport option was turned on and particles exiting the top boundary were transported according to DIVIMP predictions. The inter–ELM plasma background was used and three ERO cases were run, as in the previous section.

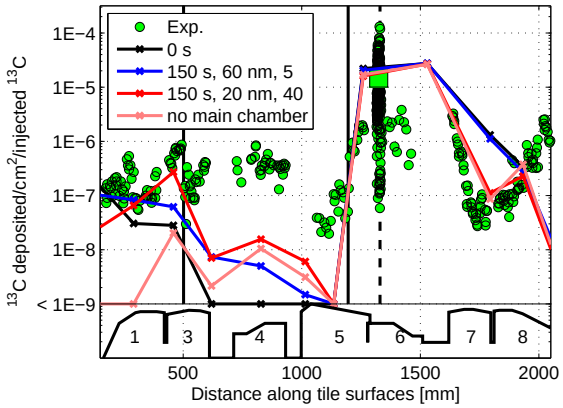

Figure 12: Initial deposition including main chamber transport for the inter ELM plasma background (black). Deposition after 150 s of erosion and re-deposition is shown for the case with low re-erosion (blue) and and the case with high re-erosion (red). The high re-erosion curve for the case without main chamber transport is shown for comparison (pink).

Including the main chamber transport increased the deposition at the inner target and the private flux region by a factor of 3 — 100 (fig. 12). Figure 12 shows the primary deposition (no re-erosion) as well as the resulting deposition after 150 seconds for the inter-ELM plasma background for low re-erosion rates (60 nm interaction layer, enhanced re-erosion of 5) and high re-erosion rates (20 nm and 40). The increased inner target deposition is due to transport via the main SOL and core. This can be seen in figure 13 (A), where the flux of injected carbon is shown. However, the direct flux of injected carbon from the valve to the private flux region remains very small. The increase in PFR deposition is due to the increased inner target deposition and subsequent erosion in the inner target. The flux of eroded wall carbon is shown in figure 13 (B).

The outer target deposition is marginally increased because particles entering the main SOL can re-enter and deposit at the outer target. This effect is, however, small indicating that the deposition at the outer target is primarily explained by ^{13}C particles depositing in areas close to the injection valve.

Including the main chamber transport did not significantly affect the fluxes of eroded wall carbon. This can be seen by comparing figures 10 and 13. The reason for this is that material migration due to erosion seems to be dominated by short scale walking processes. Approximately 2 % of all the wall carbon

eroded in the ERO simulation volume reaches the top boundary.

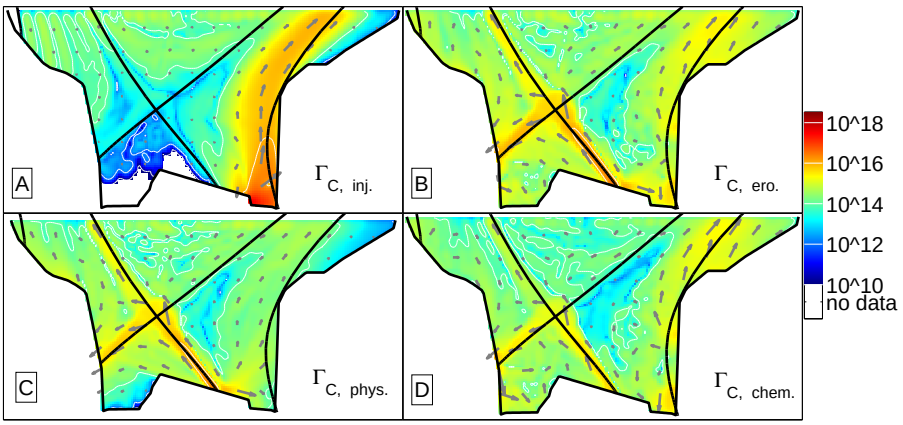

Figure 13: Fluxes of (A) injected carbon, (B) eroded wall carbon, (C) physically eroded wall carbon, and (D) chemically eroded wall carbon for the base case including main SOL and core transport. In contrast to figure 10 A, the flux of injected carbon now reaches the inner target.

Migration close to the inner strike point can be described by two processes. In the SOL, neutral carbon atoms are eroded via chemical and physical erosion (fig. 14 (A)), are ionized, and transported back to the target along the magnetic field lines. Due to the target geometry and the magnetic geometry, the eroded particle is likely to be transported towards the separatrix. This typical walking process can be clearly seen in figure 14 (B) where the flux of eroded wall carbon makes a loop in the inner target SOL. For the sparse and cool PFR plasma, neutral eroded carbon atoms can fly all the way from the inner target (tile 3) to the private flux region (tiles 4 and 5), as seen in figure 14 (A).

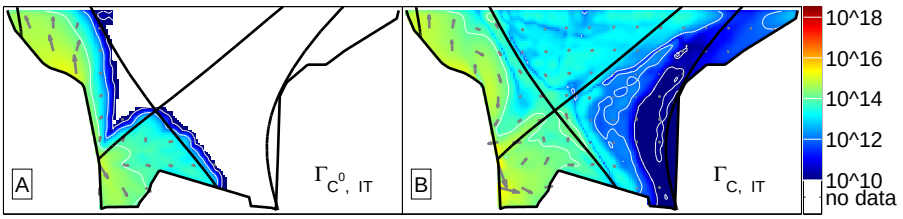

Figure 14: Flux of eroded carbon originating from the inner divertor. Figure A shows only neutral carbon and figure B includes all charge states. The fluxes of neutral carbon turn into fluxes of higher charge state carbon when coming into contact with hot plasma closer to the core.

All of the simulation are unable to match the experimental deposition at the

very end of tile 8. This is due to computational limitations as particles exiting the ERO simulation volume outside the DIVIMP grid are lost.

Similarities between these experiments in JET and experiments carried out in JT-60U [40] should be mentioned. In [40], methane was injected from the outer target from where it also migrated to the inner target. The results in [40] suggested transport due to flows in the private flux region. These flows are present in these simulations as well, and can be seen in the flux of eroded wall carbon. However, very few of the injected test particles reach the private flux region by crossing the separatrix close to the injection location in these simulations. This is explained by the direction of the walking process in these simulations. The poloidal angle between the magnetic field lines and the material surfaces close to the outer strike point are such that eroded material migrate away from the separatrix and the private flux region. In the JT-60U experiment, the direction of this walking process was the other way around.

3.3 The effect of ELMs

To address ELMs, ERO was run using inter–ELM, ELM peak, and ELM recovery plasma backgrounds. The plasma backgrounds were continuously switched during the 150 s simulation to simulate the cyclic process. The relative lengths of the time steps were 1:0.071:0.71 for the inter ELM, ELM onset, and ELM recovery time slices. As in the two previous sections, three cases were run: low re–erosion, medium re–erosion, and high re–erosion.

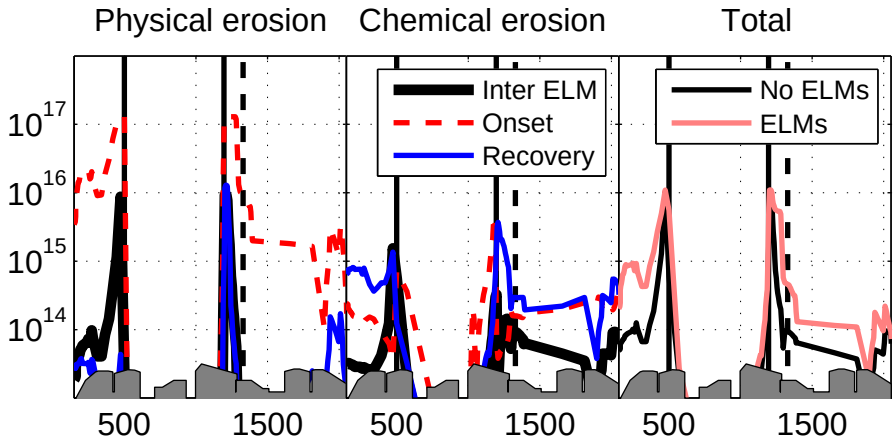

Figure 15: The physical and chemical erosion rates [atoms/cm^2/s] for inter ELM base (solid black), ELM onset (dashed red), and ELM recovery (dotted green) phases. The last figure shows the time averaged erosion rate without (black) and with (red) ELMs. The divertor tiles are shown at the bottom.

Including ELMs substantially increases the erosion rate in the far SOL of the inner and outer targets. The erosion rates for the divertor are shown in

figure 15 for the inter-ELM, the ELM onset, and ELM recovery phases. The erosion rate at the strike points is considerably larger during the ELM onset, but this time period is short compared to the inter-ELM and ELM recovery periods. Specifically, the divertor cools down and get more dense during the ELM recovery period decreasing physical erosion. Chemical erosion, on the other hand, is elevated during the ELM recovery period.

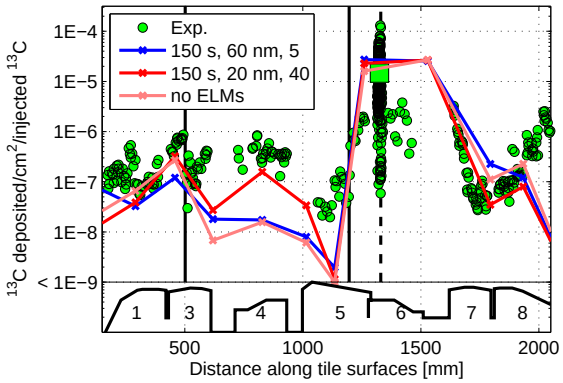

Figure 16: Deposition profile after 150s including ELMs for low erosion rates (blue) and high rates (red). The simulation case without ELMs and high erosion rates is shown for comparison (pink).

The increased erosion rates significantly affected the final deposition profile, especially in the private flux region (fig. 16). Increased erosion at the inner target increased private flux deposition making the results more consistent with experimental measurements. On the other hand, the increased re-erosion also reduced the inner divertor deposition away from the measurement.

3.4 Sensitivity analysis of the external transport option

Although the simulations were able to identify key transport mechanisms, they were unable to quantitatively explain the experimentally observed deposition pattern. There are, however, known limitations in the used models. A typical example is the parallel flow profile typically produced by EDGE2D and other fluid codes. Experimentally, a strong flow from the LFS to the HFS is seen while fluid codes typically predict stagnant flow in the main chamber SOL, and similar plasma conditions in the HFS and LFS SOL. Underestimating the flow will reduce inner target deposition and increase main chamber and outer target deposition.

Another factor increasing the main chamber deposition and underestimating inner target deposition is the narrow computational grid in DIVIMP: there is a significant gap between the outer grid boundary and the first wall as can be seen in figure 2. This had two effects in the simulations. Firstly, particles exiting the

top boundary of the ERO simulation volume at locations not covered by the DIVIMP grid were automatically lost and could not be simulated in DIVIMP. Secondly, the particles that were simulated by DIVIMP were more likely to be deposited in the main chamber in DIVIMP simply due to fact that the grid did not extend to the wall. In reality, a particle would have a finite probability of re-entering the volume covered by the grid. Approximately 5 % of the injected particles and 2 % of the eroded particles reach the boundary. Even if is this number is small, it is important for the deposition at the inner target and the private flux region considering that approximately 90 % is deposited close to the injection valve at the inner target and outer baffle.

To shed light on this issue, the number of particles depositing in the main chamber was artificially reduced in an ad hoc fashion. In this test case particles exiting the top boundary of the simulation volume, in those areas covered by the DIVIMP grid, had a constant 95 % probability of re-entering the simulation volume in ERO. The relative probability distribution was not changed. This way, the amount of particles deposited in the main chamber in the simulations dropped from around 5 % to around 2 %. The experimental value was in the order of 1 % of the found ^{13}C making this ad-hoc "fix" justifiable. A similar method was also utilized in publication [2].

Enhancing poloidal main chamber transport increased the amount of particles reaching the inner target and subsequently the amount of particles reaching the private flux region. Figure 17 shows the deposition profile after 150 s of injection and erosion for the simulation with ELMS and increased main chamber transport for low and high re–erosion as well as the high re–erosion case without enhanced main chamber transport. This ad hoc fix made the predictions more consistent with the measured deposition profiles.

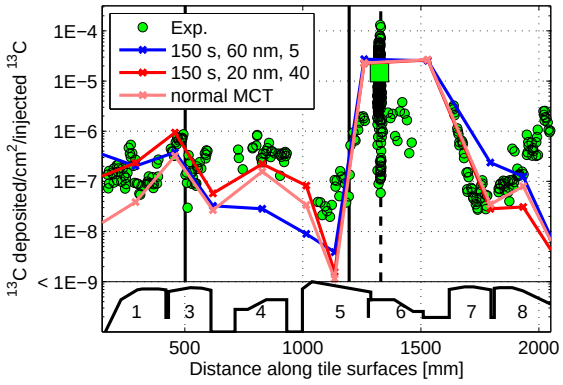

Figure 17: Deposition profiles after 150 s with enhanced main chamber transport (MCT) for high re-erosion rates (red) and low re-erosion rates (blue). The high re-erosion rates case without enhanced main chamber transport is shown for comparison (pink).

The effect of artificially imposing a SOL background flow was also tested, as has been done in several studies [41][42][43]. In [41], a mach number of 0.5 towards the inner target was imposed for the main chamber SOL. Here, a mach number of 0.5 was imposed in the main chamber SOL above the ERO simulation volume and DIVIMP was used to generate the corresponding transport matrix. The imposed flow studies were only done for the inter–ELM plasma background since it is not obvious how the SOL flow behaves during the ELM cycle.

Imposing the artificial flow in the main chamber SOL increased the likelyhood of particles reaching the inner target compared to the base case inter–ELM simulations (fig. 18). This results is consistent with [41]. Increased inner target deposition also increased the private flux region deposition via erosion at the inner target. However, the inter–ELM simulations with the imposed flow were not able to produce the same amount of private flux region deposition as the simulations with the ELMs.

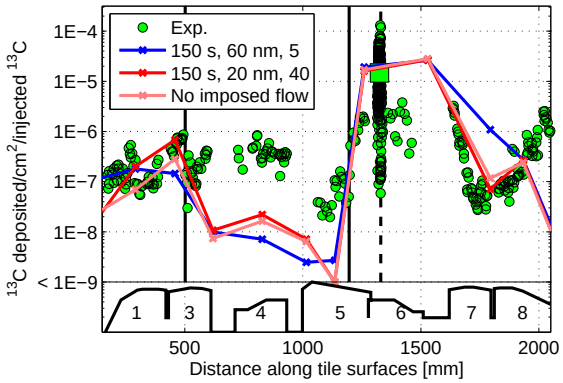

Figure 18: Deposition profiles after 150 s with enhanced main chamber background flow for high re-erosion rates (red) and low re-erosion rates (blue). The high re-erosion rates case without enhanced main chamber background is shown for comparison (pink). These simulation cases do not include ELMs.

4 Conclusions

The 2009 carbon tracer experiment in JET was simulated with a combination of EDGE2D-EIRENE, ERO and DIVIMP. ERO and DIVIMP were combined by a new external transport option in ERO were particles exiting the simulation volume in ERO could return with a given probability distribution. This probability data was calculated using DIVIMP.

Experimentally, the carbon was injected at the outer target from where it migrated to the inner target and private flux region. A large fraction was also deposited close to the injection valve. The simulations using the inter-ELM

plasma background identified several key pathways for injected ^{13}C: transport from the outer target to the inner target via the main SOL and core, and erosion at the inner target leading to migration of ^{13}C towards the private flux region. Transport across the divertor alone was approximately two or three orders of magnitude too low to explain the measured inner target and private flux region profiles. Including the main chamber transport was crucial in explaining the lower divertor deposition in these experiments. However, simulation using this setup were not able to reproduce the private flux region deposition. The simulation cases with the highest amount of re–erosion, and best match in the private flux region, predicted approximately one order of magnitude too low ^{13}C concentration.

To understand the role of ELMs, a simple ELM model was implemented. The diffusion coefficient in EDGE2D was artificially increased for a short period and the resulting plasma background was used in ERO and DIVIMP. Including ELMs increased the deposition in the private flux region by an order of magnitude due to larger re–erosion rates and was the key to bringing carbon to the private flux region.

The simulations varied parameters related to erosion yields in ERO. The interaction layer depth was varied from 60 nm to 20 nm and the enhanced re-erosion factor was varied from 5 to 40. Re–erosion was crucial to explain the experimental deposition pattern. Furthermore, The cases with the highest amount of erosion (interaction layer of 20 nm and enhanced re-erosion of 40) were closest to the experimental values for all setups. The simulation case with ELMs and the highest amount of re–erosion provided a reasonable match to experimental data but still slightly underestimating the deposition at the inner target and the PFR.

Limitations in the simulation model due to a spatially restricted computational grid and the predicted SOL background flow were studied. The effect of the restricted grid was studied by artifically modifying transport in the main chamber leading to a more realistic deposition prediction. Also, the effect of imposing a flow into the SOL background plasma was tested. In line with previous work, imposing the flow increased the deposition at the inner target.

Future work should address a a number of issues that could not be addressed in this work. The injection of methane cools the plasma locally. The density of carbon eroded from the material surfaces is larger than that of injected in most parts of the lower divertor. However, this is not the case close to the injection location. Another, diagnostic method that was experimentaly available but not utilized in this work is given by the fact that the injected methane contained hydrogen while the plasma background was deuterium. Spectroscopically, a CH–layer was observed groving during the discharges. The simulations in this paper did not follow the injected hydrogen — only the carbon. Furthermore, transient effects at the beginning and end of discharges, such as strike point movement, can play a role in the final deposition pattern.

5 Acknowledgements

This work has been carried out within the framework of the EUROfusion Consortium and has received funding from the Euratom research and training programme 2014-2018 under grant agreement No 633053 and from Tekes the Finnish Funding Agency for Innovation under the FinnFusion Consortium. The views and opinions expressed herein do not necessarily reflect those of the European Commission

References

[1] P.C. Stangeby J. Nucl. Mater. **415** (2011) S278 — S283

[2] A. Hakola et al. Contrib. Plasma Phys. **55** (2013) 124029

[3] D.M. Goebel et al. Nucl. Fusion **28** (1988) 1041

[4] J. Roth J. Nucl. Mater. **266—269** (1999) 51—57

[5] S. Brezinsek et al. J. Nucl. Mater. **363—365** (2007) 1119—1128

[6] A. Kreter el at. Plasma Phys. Control. Fusion **50** (2008) 095008

[7] N. Asakura J. Nucl. Mater. **363—365** (2007) 41—51

[8] J. Miettunen et al. Nucl. Fusion **52** (2012) 032001

[9] U. Kgler et al. J. Nucl. Mater **241** — **243** (1997) 816

[10] J.D. Strachan et al. Nucl. Fusion **43** (2003) 922

[11] A. Hakola et al. Plasma Phys. Control. Fusion **52** (2010) 06500

[12] P. Petersen et al. Phys. Scr. **2014** (2014) 014042

[13] S.L. Allen et al. J. Nucl. Mater. **337—339** (2005) 30

[14] Y. Ueda et al. Nucl. Fusion **49** (2009) 065027

[15] J. Likonen et al. Phys. Scr. **T145** (2011) 014004

[16] J.P. Coad et al. Phys. Scr, **2011** (2011) 014003

[17] A. Kirschner et al. Nucl. Fusion **40** (2000) 989

[18] P.C. Stangeby, J.D. Elder Nucl. Fusion **35** (1995) 13911412

[19] R. Simonini Contrib. Plasma Phys. **34** (1994) 36873

[20] D. Reiter D et al. Fusion Sci. Tech. **47** (2005) 17286

[21] EDGE2D/EIRENE code interface report, JET ITC-Report, http://www.eirene.de/e2deir_report_30jun06.pdf, 2006

[22] W. Eckstein et al. Sputtering by particle Bombardment, Springer Publishing, (2007)

[23] J. Roth et al., J. Nucl. Mater. 337 339 (2005) 970 — 974.

[24] M. Groth et al. IAEA FEC (2014)

[25] S. Wiesen et al. Plasma Phys. Control. Fusion **53** (2011) 124039 — 124050

[26] D. Harting et al. J. Nucl. Mater. (2014) in Press

[27] L. Aho-Mantila et al., IAEA FEC (2014)

[28] J.D. Strachan et al. Nucl. Fusion **48** (2008) 105002

[29] M.I. Airila et al. Europhysics Conf. Abs. (2013) 37D P2.126

[30] K. Schmid et al. J. Nucl. Mater, **415** (2011) 284

[31] Janev R and Reiter D 2002 Collision Processes of Hydrocarbon Species in Hydrogen Plasmas: l. The Methane Family, Report Jul-3966, ISSN 0944-2952

[32] Summers, H. P. (2004) The ADAS User Manual, version 2.6 http://www.adas.ac.uk

[33] A. Kirschner Fusion Science and Technology **57** (2010) 277—292

[34] A. Kirschner et al. J. Nucl. Mater **328** (2004)

[35] A. Kirschner et al. J. Nucl. Mater **415** (2011)

[36] M.I Airila et al. Phys. Scr. **2009** (2009) 014021

[37] R. J. Fonck et al. Phys. Rev. Lett. **49** (1982) 737

[38] T. Makkonen et al. Phys. Scr. **90** (2015) 015204

[39] T. Makkonen et al. Comp. Phyc. Comm. **184** (2013) 1842 — 1847

[40] Y. Nobuta et al. 34th EPS Conference on Plasma Phys. Warsaw, 2 - 6 July 2007 ECA Vol.31F (2007) P-1.024

[41] J. Miettunen et al. Plasma Phys. Control. Fusion **56** (2014) 095029

[42] T. Makkonen et al. J. Nucl. Mater. **415** (2011) S479 — S482

[43] J.D. Elder et al. J. Nucl. Mater. **363** (2007) 140 — 145